

Dust evolution in a supernova interacting with the ISM

Evgenii O. Vasiliev¹, Yuri A. Shchekinov²

¹*Lebedev Physical Institute, Russian Academy of Sciences, 53 Leninsky Avenue, Moscow 119991;*

²*Raman Research Institute, Sadashiva Nagar, Bangalore 560080, India;*

Accepted XXX. Received YYY; in original form ZZZ

ABSTRACT

Supernovae (SN) explosions are thought to be an important source of dust in galaxies. At the same time strong shocks from SNe are known as an efficient mechanism of dust destruction via thermal and kinetic sputtering. A critically important question of how these two hypotheses of SNe activity control the dust budget in galaxies is still not quite clearly understood. In this paper we address this question within 3D multi-fluid hydrodynamical simulations, treating separately the SNe injected dust and the dust pre-existed in ambient interstellar gas. We focus primarily on how the injected and pre-existed dust are destroyed by shock waves and the hot gas in the SN bubble depending of the density of ambient gas. Within our model we estimate an upper limit of the SN-produced dust mass which can be supplied into interstellar medium. For a SN progenitor mass of $30 M_{\odot}$ and the ejected dust mass $M_d = 1 M_{\odot}$ we constrain the dust mass that can delivered into the ISM as $\geq 0.13 M_{\odot}$ provided the injected dust particles are large $a \geq 0.1 \mu\text{m}$.

Key words: Interstellar dust; Interstellar dust processes; Supernova remnants

1 INTRODUCTION

Dust is an important constituent of the interstellar medium (ISM), playing key role in physical processes that determine its basic properties: chemical transformations, metal budget in gas phase, thermodynamic state, radiation transfer. Dust is known to convert stellar light and thermal energy of hot gas in infrared (IR) radiation. One of the intriguing questions concerns the dust mass budget in the ISM (see for recent discussion in [Mattsson 2021](#); [Kirchschlager et al. 2022](#); [Péroux et al. 2023](#)). The interrelation between the destruction and production dust rate in the ISM is still not quite well understood. Particular concern are the metamorphosis the dust particles undergo behind the strong shock waves, $v_s \gtrsim 150 \text{ km s}^{-1}$, penetrating the ISM. It is generally thought that dust particles experience efficient destruction from such shocks and from the hot gas behind them. The three processes dominate the dust destruction: the inertial and the thermal sputtering ([Draine & Salpeter 1979b,a](#); [Nath et al. 2008](#); [Slavin et al. 2015](#); [Priestley et al. 2022](#), and references therein), and the shattering in grain-grain collisions at higher densities ([Jones et al. 1996](#); [Kirchschlager et al. 2019](#)). Theoretical considerations show that the characteristic dust lifetime in the Milky Way ISM against sputtering is $t_{sp} \lesssim 3 \times 10^8 \text{ yr}$, resulting in the decrease rate $\dot{M}_d^- \lesssim 0.1 M_{\odot} \text{ yr}^{-1}$ ([McKee 1989](#), and for more recent discussion ([Micelotta et al. 2018](#); [Ferrara & Peroux 2021](#))). On the other hand, the overall production rate from red giants winds and SNe explosions is $\dot{M}_d^+ \sim 10^{-3} \text{ SFR} M_{\odot} \text{ yr}^{-1}$, where $\text{SFR} \sim 5 M_{\odot} \text{ yr}^{-1}$, indicating a crying disbalance between the dust destruction and its replenishment ([Draine 2009](#)).

Recent measurements of abundance patterns in supernovae remnants (SNR) in the Milky Way (MW) and Large Magellanic Clouds (LMC) with strong non-radiative shocks, $v_s \approx 350 - 2700 \text{ km s}^{-1}$, have constrained the destroyed dust fraction by $\lesssim 0.1 - 0.6$, even in a rather dense environment (see Tables 1 and 3 in [Zhu et al. 2019](#)). One can think, therefore, that older SNRs with weaker shock waves

are less destructive that commonly thought. More recent observations of three SNRs in the MW do apparently confirm such a conclusion ([Priestley et al. 2021](#)).

Another issue is connected with survival of dust particles born in SNe ejecta ([Bocchio et al. 2016](#)). Observation of dust in high-redshift ($z \gtrsim 5$) galaxies and quasars ([Bertoldi et al. 2003](#); [Maiolino et al. 2004](#); [Beelen et al. 2006](#); [Dwek & Cherchneff 2011](#); [Gall et al. 2011](#)) brought direct and convincing arguments that SNe ejecta can be a very efficient source of dust in the universe. Direct IR observations also show that dust can be produced at early stages of the ejecta outflows as manifested in several nearby SN remnants ([Gomez et al. 2012](#); [Arendt et al. 2014](#)), in SN1987A ([Indebetouw et al. 2014](#); [Matsuura et al. 2015](#)), and in the local group galaxy NGC 628 ([Sugerman et al. 2006](#)). More recent analysis of IR characteristics from SN1897A ([Wesson & Bevan 2021](#)) indicates that dust forms in SNe ejecta at latter stages $\gtrsim 1000$ days.

The total dust mass supplied by a SN in the ISM, and the dust size distribution sensitively depend not only on the progenitor mass, but on the density of ambient gas as well, because of the reverse shock from the interaction of the ejecta with the ambient gas. 1D simulations by [Nozawa et al. \(2006, 2007\)](#); [Bianchi & Schneider \(2007\)](#); [Nath et al. \(2008\)](#) have shown that increase of the ambient gas density from 0.1 to 10 cm^{-3} can result in a drop of dust yield by one to two orders, particularly for higher progenitor masses. Not less important is the conclusion that destruction of small size dust by the reverse shock considerably flattens the size spectrum. More recently, theoretical analysis of dust destruction in the process of interaction of the ejecta with ambient ISM lead [Slavin et al. \(2020\)](#) to conclude that when possible relative motion of dust particles with respect to gas is accounted, the heavier dust particles can penetrate the region affected by the reverse shock and can escape relatively intact into the ambient ISM gas. However, eventually a fraction of them is becoming

destroyed *in situ* in the surrounding ambient gas: the silicate particles are found, as expected, to experience nearly as twice stronger destruction as the carbonaceous ones.

This result suggests that the SN explosions supply in the ISM dust particles of predominantly large sizes. This on its turn can contribute to variations of the extinction law on smaller scales unless dust particles are well mixed with dust in ambient gas. The mixing begins in fact on earlier stages, around a few thousands years when a fraction of large size particles overcomes the forward shock and penetrate the ambient ISM, as mentioned by [Slavin et al. \(2020\)](#). As a consequence, the signatures of such local inhomogeneities in extinction law can manifest in the ISM in the Milky Way and other galaxies as well. Such variations may in principle appear even on larger scales in the ISM, as have been described first by [Fitzpatrick & Massa \(1990\)](#).

2 MODEL DESCRIPTION

We consider the dynamics and destruction of dust particles in a supernova remnant during its 300 kyr-long interaction with a slightly inhomogeneous clumpy ISM. We use our gasdynamic code ([Vasiliev et al. 2015, 2017](#)) based on the unsplit total variation diminishing (TVD) approach that provides high-resolution capturing of shocks and prevents unphysical oscillations, and the Monotonic Upstream-Centered Scheme for Conservation Laws (MUSCL)-Hancock scheme with the Haarten-Lax-van Leer-Contact (HLLC) method (see e.g. [Toro 2009](#)) as approximate Riemann solver. This code has successfully passed the whole set of tests proposed in [Klingenberg et al. \(2007\)](#). In order to follow the dynamics of dust particles we have implemented the method similar to that proposed by [Youdin & Johansen \(2007\)](#), [Mignone et al. \(2019\)](#) and [Moseley et al. \(2023\)](#). A description and tests are given in Appendix. We take into account the destruction of dust particles by both thermal (in a hot gas) and kinetic (due to a relative motion between gas and grains) sputtering ([Draine & Salpeter 1979a](#)). The backward reaction of dust on to gas due to momentum transfer from dust particles is also accounted in order to ensure dynamical self-consistency. This effect can be of importance in correct estimates of the kinetic sputtering for particles inertially entering the ambient gas at the interface between the bubble interior and the surrounding gas.

The gas distribution in the ambient (background) medium is set to be a slightly inhomogeneous medium with averaged number density n_b and small-size low-amplitude density fluctuations $\delta r \sim 2 - 3$ pc, $\delta n/n_b \sim 0.1$. The fluctuations are constructed by using module pyFC¹ ([Lewis & Austin 2002](#)) which generates lognormal “fractal cubes” for gas density field. The averaged ambient density is equal to $n_b = 1 \text{ cm}^{-3}$ as a fiducial value, we calculate also models with 0.1, 0.3, 3 and 10 cm^{-3} , the temperature in all models is 10^4 K . Initially the gas pressure is assumed uniform over the grid. The metallicity of the background gas is usually set to the solar value, $[Z/H] = 0$. We assume a dust-to-gas (DtG) mass ratio equal to $\zeta_b = 10^{-2} [Z/H]$.

We inject the mass and energy of a SN in a region of radius $r_0 = 3$ pc, assuming commonly used values $30 M_\odot$ and 10^{51} erg. The energy is injected in thermal form. The injected masses of metals and dust are $10 M_\odot$ and $1 M_\odot$, correspondingly. Dust particles are thought to start growing during the free expansion phase of a SN evolution on much earlier times, when the ejecta temperature drops to several thousand Kelvins (e.g. [Todini & Ferrara 2001](#)), typically after $\gtrsim 300$ days when the ejecta radius is of ~ 0.03 pc. At

this age the characteristic time of dust-gas collisional coupling (the stopping time, see Sec. A2) for the parameters within the ejecta is $\tau_s \sim 10^6 n^{-1} a_{0.1} \text{ s}$, with $a_{0.1}$ being the dust grain radius in $0.1 \mu\text{m}$. For $M_{ej} = 30 M_\odot$, and $r_0 = 3$ pc, the ejecta gas density $n \sim 10^3 \text{ cm}^{-3}$, resulting in $\tau_s \sim 10^3 a_{0.1} \text{ s}$ at gas temperatures typical for dust growth. This suggests that the injected dust particles are involved into the ejecta outflow on a short time scale. In the process of this acceleration a fraction of dust particles can experience kinetic sputtering ([Slavin et al. 2020](#), see also estimates in Sec. A4), whereas thermal sputtering remains weak because of a low temperature in ejecta $T < 6000 \text{ K}$. Thermal sputtering increases when the ejecta meets the reverse shock and becomes thermalized at $t \sim 300 \text{ yr}$ ([Nozawa et al. 2007](#); [Nath et al. 2008](#); [Slavin et al. 2020](#)). Overall, at $t \geq 300 - 400 \text{ yr}$ the destroyed dust mass fraction can vary from 0.3 to 0.8 depending on hydrodynamical field in the surrounding gas ([Slavin et al. 2020](#)). In this sense the estimates of the contribution of dust supply into the ISM from SNe explosions presented in our model can be regarded as upper limits.

The mass of dust is redistributed between many dust ‘superparticles’. For instance, in case the number of dust ‘superparticle’ is 2^{20} , the mass of each dust ‘superparticle’ is $\sim 1 M_\odot / 10^6 \sim 10^{-6} M_\odot$ for the monodisperse dust of total mass equal to $1 M_\odot$. In the equation of motion of dust we attribute to a single grain the mass and the size of physical dust particles, while in the momentum equation for the gas component the momentum from dust is treated as a sum of momentum from all dust grains that constitute the dust mass $\sim 10^{-6} M_\odot$ allocated in a cell.

Here we consider primarily a monodisperse (a single size) dust. We perform a set of independent runs for different monodisperse sorts of dust with initial sizes equal to $a_0 = 0.03, 0.05, 0.1, 0.3, 0.5 \mu\text{m}$; $a_0 = 0.1 \mu\text{m}$ is the fiducial value. During the evolution dust grains are destroyed and their sizes decrease depending on physical conditions in ambient gas; the minimum size is set to $0.01 \mu\text{m}$. We adopt the same initial distribution of sizes both for the dust pre-existed in ambient gas (referred hereinafter as the background dust) and for the injected dust. We assume that the mass of metals produced due to sputtering is returned to the gaseous phase. Evolution of polydisperse dust will be described elsewhere.

In our models the spatial resolution is set to 0.5 pc, that is sufficient for adequate treatment of dynamics of a SN bubble in a medium with density $n_b \sim 0.1 - 10 \text{ cm}^{-3}$. In particular, in a medium with $n_b = 1 \text{ cm}^{-3}$ we follow the SN bubble evolution until late radiative phase: $t_{end} \sim 10 t_{cool} \sim 300 \text{ kyr}$, when its radius reaches around $\simeq 40 \text{ pc}$. Therefore, we set the size of the computational domain $(96 \text{ pc})^3$, with the number of cells 192^3 . We set one dust ‘superparticle’ per a computational cell resulting in the total number of background dust particles in the domain $192^3 \sim 7$ millions. The fiducial number of injected ‘superparticles’ per SN is $2^{23} \sim 8$ millions. Our choice of both grid resolution and number of the injected particles is justified by our tests presented in Appendix B2. Note that in dynamical regime dust particles can escape their initial “mother” cells and move into other neighbour ones. As a result, depending on gas density the overall distribution of dust particles can be rather patchy and can manifest in lack and/or deficient dust particles at certain volumes of the bubble or on averaged radial profiles, see in Sec. B3.

Simulations are run with tabulated non-equilibrium cooling rates fitting the calculated ones for a gas that cools isochorically from 10^8 down to 10 K ([Vasiliev 2011, 2013](#)). The heating rate is assumed to be constant, with a value chosen such as to stabilize the radiative cooling of the ambient gas at $T = 10^4 \text{ K}$.

¹ The code is available at <https://bitbucket.org/pandante/pyfc/src/master/>

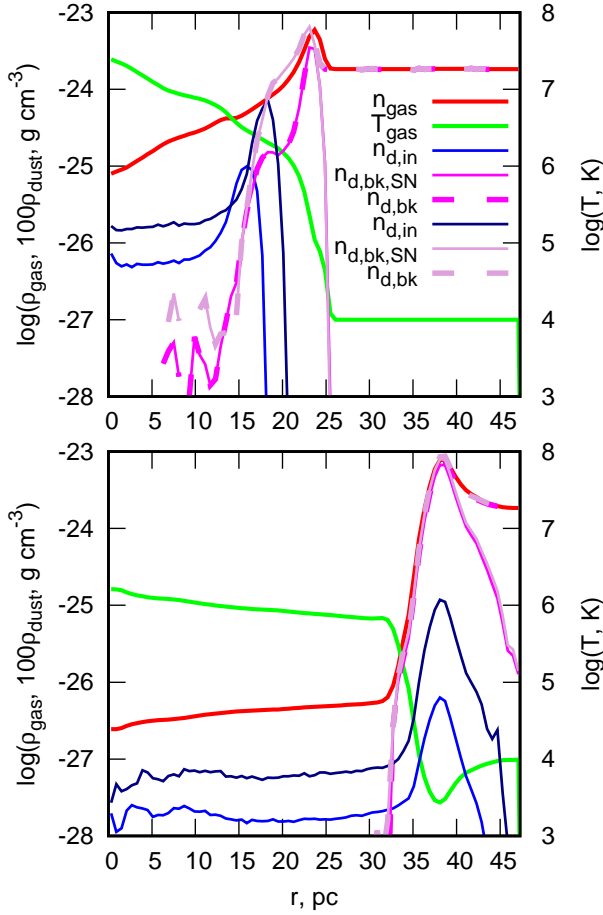


Figure 1. The averaged radial profiles of gas density, gas temperature, injected and background dust particles as legended, at 50 and 300 kyr from top to bottom, respectively: solid pink line shows separately evolution of the background dust particles as they penetrate behind the shock, solid light-pink line shows the background dust behind the shock without sputtering; solid dark-blue line shows the injected dust without sputtering, for solid blue line sputtering is accounted. The initial grain size is equal to the fiducial value: $a_0 = 0.1 \mu\text{m}$.

3 DYNAMICS

3.1 Dust radial distribution

Inside a SN bubble dust is efficiently destroyed by both the thermal and kinetic sputtering (Draine & Salpeter 1979a). The contribution from the latter for background dust particles in a magnetic-free case is around 15%, while for the injected ones it is even smaller because of a lower drift between the gas and dust². Fig. 1 presents angle averaged radial profiles for gas density and temperature, and densities of both sorts of dust particles – the SN injected and the background dust, for the fiducial grain size at 50 and 300 kyr after the SN has exploded. Because of an initially introduced clumpy density distribution and partly because of a growing Rayleigh-Taylor (RT) instability the averaged shock layers in $n(r)$ and T are wider than typical. At $t = 50$ kyr the injected dust remains ~ 7 pc deeper behind the shock and remains partly survived – by 10%, within the central ~ 10 pc interior. The background dust is swept by the shock and penetrates behind it by ~ 5 pc inwards, but only within a $\sim 2 - 3$ pc thick layer it

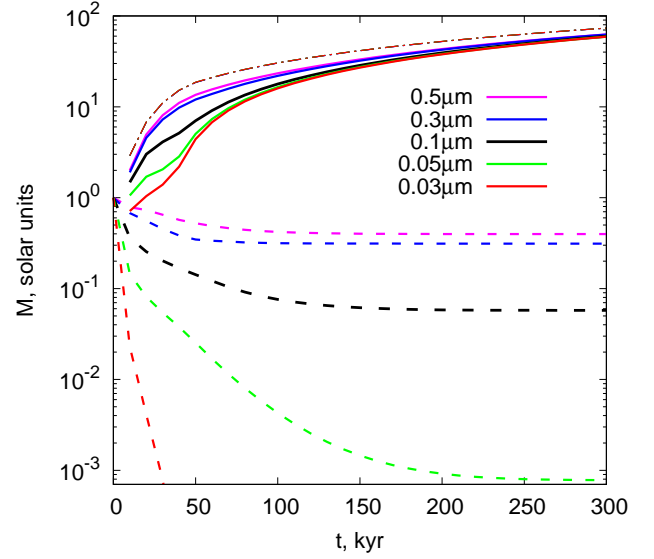


Figure 2. The total mass of dust involved into the SN bubble till a given time. Solid lines show the evolution of the background dust (pre-existed in the ambient gas), dashed lines depict the evolution of the injected dust, dot-dashed red line shows the mass of the same dust without destruction.

survives within factor of 2, as seen from comparison of the pink (sputtering accounted) and the light-pink (no sputtering is included) lines in upper panel of Fig. 1. At 300 kyr only a small fraction of injected dust survives within the bubble interior, around 10% if it penetrates ahead of the forward shock³. At the same time, some of the background dust particles are seen to overcome the averaged front apparently after being accelerated in RT advancing “tongues” and penetrated outward. Behind the front their density drops within $\delta r \lesssim 5$ pc inwards the bubble. Details are shown in Fig. 8 in Sec. B3.

3.1.1 Background dust

The background grains in the swept up gas of the SN shell are destroyed efficiently during the early expansion $t \lesssim 50$ kyr. This can be observed in upper panel ($t = 50$ kyr) of Fig. 1, where dust destruction is lower in the immediate post-shock region, whereas in deeper and hotter domain remains considerable. The reason is that dust particles of radius $a \gtrsim 0.1 \mu\text{m}$ are destroyed with characteristic time $t \sim 10^2 n^{-1} a_{0.1}$ kyr comparable to radiative cooling time $t_{\text{cool}} \sim 10^2 n^{-1}$ kyr. As at $t \sim 30$ kyr the remnant enters the radiation dominated phase dust destruction on later times weakens. Solid lines in Fig. 2 depict the mass of the background dust involved into the SN bubble. For comparison, dot-dashed red line shows the mass of the same dust without destruction. On longer time sputtering ceases, and asymptotically the swept up dust mass grows proportionally to $\propto R_s^3 \sim t^{3/4}$.

3.1.2 Injected dust

Figure 2 shows evolution of the total mass of dust populations of different sizes injected into the SN bubble. Small injected particles are destroyed quickly with characteristic sputtering time $\propto a$, e.g. grains of initial size $0.03 \mu\text{m}$ are almost completely sputtered within 10 kyr after SN explosion. During further evolution the shock velocity

² Details are given in Appendix A4.

³ This is also observed in the model by Slavin et al. (2020).

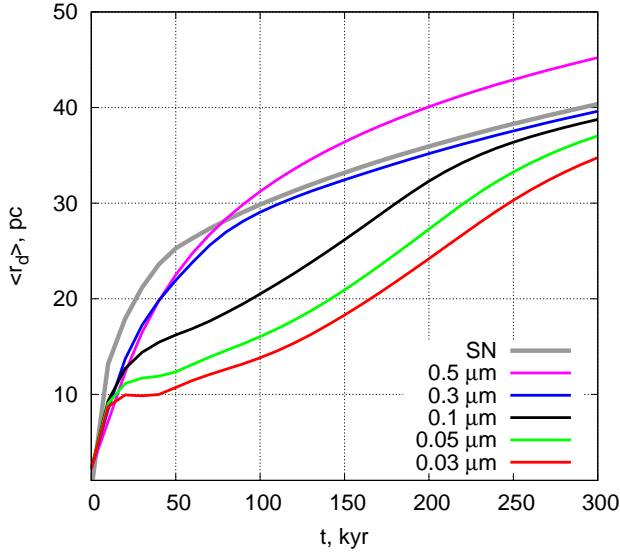


Figure 3. The averaged distance $\langle r_{a_0}(t) \rangle$ of ensembles of the injected dust particles with the initial radii $a_0 = 0.03 \mu\text{m}$ to $0.5 \mu\text{m}$ as shown in legend from the injection point. Color lines mark $\langle r_{a_0}(t) \rangle$ for an ensemble corresponding to a given a_0 ; thick grey line depicts the radius of the SN bubble.

and the gas temperature in the bubble and in the ejecta decrease as can be judged from Fig. 1, and consequently the efficiency of dust destruction also decreases. As a result at $t > 100$ kyr sputtering for injected particles of all sizes freezes out at the level reached at $t \sim 100$ kyr. Asymptotically the mass of survived dust is $\sim 5\%$ for particles of $a_0 = 0.1 \mu\text{m}$ to $\sim 40\%$ for $a_0 = 0.5 \mu\text{m}$.

Before going to details of dust destruction on smaller scales, let us consider first more generic averaged behavioral features. This gives us an impression about a collective dynamics of the injected particles depending on their initial radii a_0 . For this we calculate the averaged distance $\langle r_{a_0}(t) \rangle$ from the injection centre of an ensemble of those particles that are remained after destruction of particles initially having a given radius a_0 , averaging is over their variable mass spectrum. At $t \gtrsim 100$ kyr the SN remnant turns to the radiative stage and forms a relatively dense and thin shell. The injected dust particles as being surrounded from the beginning by hot gas of ejecta are destroyed mostly by thermal sputtering. The fraction of the remnant volume they occupy asymptotically at $t \geq 200$ kyr depends on the particles initial size. Fig. 3 illustrates the evolution of $\langle r_{a_0}(t) \rangle$ for different a_0 . At early times ($\lesssim 10$ kyr), during the free and Sedov-Taylor phases, the dynamics is weakly size dependent. Further evolution though turns to be sensitive to the grain size. Small light particles $a_0 < 0.1 \mu\text{m}$ are tightly coupled to the ejecta and hot bubble interior, and as such asymptotically they remain within the inner 30–36 pc of the bubble, such particles chase the dense shell till ~ 250 kyr and are stuck in the shell. On the contrary, heavier dust particles $a_0 \geq 0.1 \mu\text{m}$ reach either the SN shock layer, or even overcome it as $a_0 = 0.5 \mu\text{m}$ particles do.

3.1.3 Dust survival vs gas ambient density

Decrease of the survival fraction for the injected dust shown by dashed lines in Fig. 4 is simple to understand. Indeed, as the ambient density increases the expansion velocity of the forward SN shock lowers, and as a consequence so does the expansion velocity of the ejecta prolonging stay of the injected dust particles in a hostile

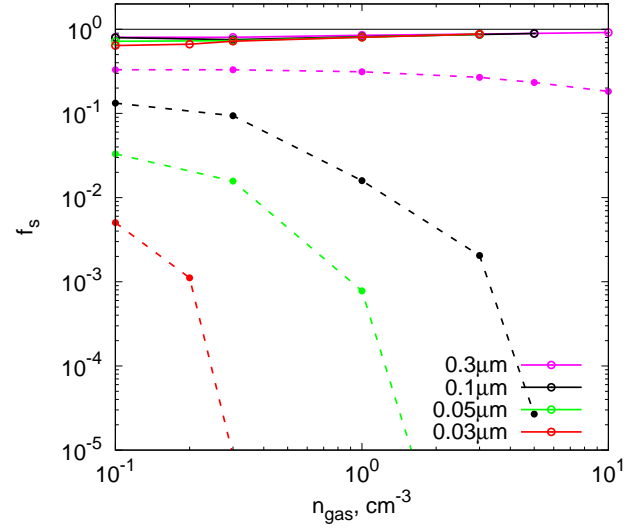


Figure 4. Dependence of survival fraction of the background (solid lines) and injected (dashed lines) dust at the asymptotics $t \geq 300$ kyr versus the ambient gas density; the horizontal thin solid line is the fraction without destruction.

ejecta environment. Even though the SN shell turns to the radiation dominated expansion in shorter time, it is sufficient for a considerable destruction of dust within the ejecta.

On the other side, the background dust is much less sensitive to the ambient density as seen in Fig. 4 by solid lines. This is connected with the fact that the characteristic destruction time by sputtering is $\tau_{\text{sp}} \sim 10^5 n^{-1} a_{0.1}$ s at gas temperature $T > 10^6$ K for $a \sim 0.1 \mu\text{m}$, is nearly equal to the gas cooling time with $Z \sim Z_{\odot}$, $t_{\text{cool}} \sim 10^5 n^{-1}$ s at $T \sim 3 \times 10^6$ K. For dust particles of $a \geq 0.03 \mu\text{m}$ the sputtering time is only ≤ 3 times shorter than cooling time. The sputtering rate degrades as $\sim T^{-3}$ below $T < 10^6$ K, resulting in simultaneous slowing of dust destruction. The gas cooling rate degrades though later, when temperature falls below $T \lesssim 10^5$ K. One can think, therefore, that sputtering is delaying with respect to gas cooling. As the SN remnant becomes radiative at $t \geq 50 n^{-1}$ kyr, the independence of the survival yield of the background dust shown in Fig. 4 is consistent with this thermal scenario. In this connection it is worth noting that the survival yield shown here is already established within the intermediate asymptotics at $t \gtrsim 50 n^{-1}$ kyr.

3.1.4 Time variation of dust sizes

Figure 5 presents evolution of the grain size distribution functions of grain sizes by mass for the injected and background particles of different initial sizes inside the SN bubble: $a_0 = 0.3, 0.1$ and $0.05 \mu\text{m}$. The size distribution function is defined as the mass fraction of grains in a given size bin $\Delta = a_i/a_{i-1}$, $\log \Delta = 0.165$ for the number of bins $N = 15$ within $0.01 - 0.3 \mu\text{m}$ is defined as

$$f_{M_d}(a_i) = \frac{M_d(a_i)_{r < R_s}}{\sum_i M_d(a_i)_{r < R_s}}, \quad (1)$$

where R_s is the bubble radius, i.e., the radius of the forward shock. Large grains are destroyed slower than the small ones proportionally to their radius $t_{\text{sp}} \propto a$. Consequently, within the first 50 kyr the injected particles with $a_0 = 0.3 \mu\text{m}$ decrease in size by less than ~ 3 times and stay unchanged further on times ≥ 100 kyr. This is consistent with the total mass of survived injected particles shown

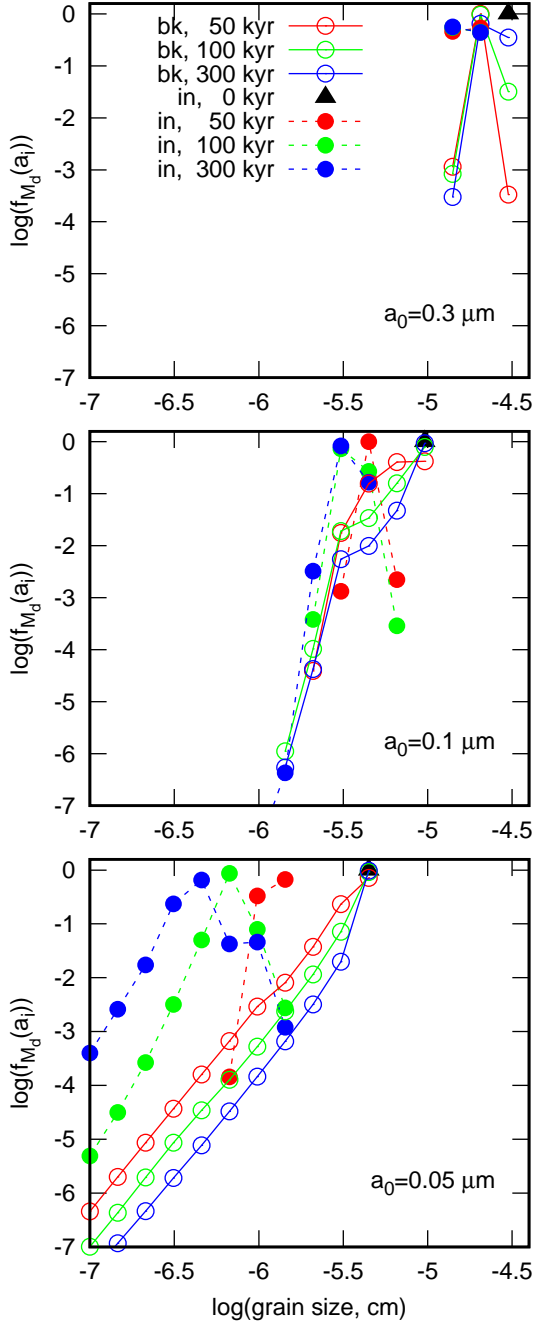


Figure 5. The mass distribution functions of grain sizes for the injected (solid circles connected solid lines) and background (open circles connected dash lines) particles of initial sizes: $a_0 = 0.3, 0.1$ and $0.05 \mu\text{m}$ from top to bottom panels, respectively, in the SN bubble with age of 50, 100 and 300 kyr (red, green and blue lines). Initially dust is monodisperse with size equal to a_0 . For the injected dust the initial distribution is marked by black solid triangle symbol. The averaged number density of the ambient gas is 1 cm^{-3} .

in Fig. 2. The background particles crossed the front are destroyed less strong, because they spend in the postshock hostile region a shorter time, and only a negligible fraction pervade into the hot bubble and the ejecta as $\tau_s/t_{\text{sound}} \approx 1$ such that dust particles are getting involved into gas flows after passing a few cells. On the other hand, at $t > 50$ kyr the postshock gas becomes radiative, gas temperature falls below $T \lesssim 10^6$ K, and correspondingly the sputtering rate $|\dot{a}|/a \propto T^3$

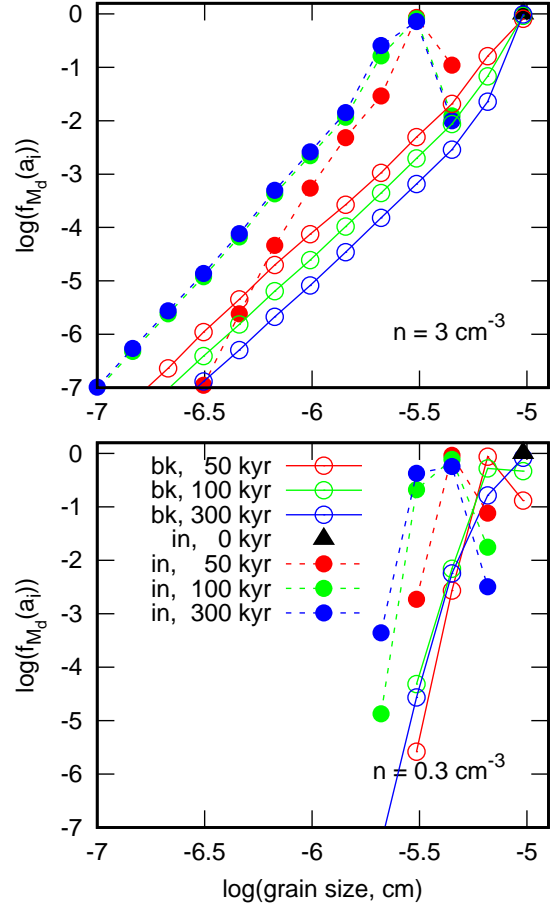


Figure 6. The same as in Figure 5, but for particles of initial size $a_0 = 0.1 \mu\text{m}$ and number densities of the ambient gas is 3 cm^{-3} (upper panel) and 0.3 cm^{-3} (lower panel).

decreases faster than the cooling rate $|\dot{T}|/T \propto T^{-1}$. After ~ 50 kyr only a minor fraction of the background dust experiences sputtering. This explains a weak growth of survived fraction of background dust with ambient density.

The injected dust grains of smaller initial sizes 0.1 and $0.05 \mu\text{m}$ are destroyed on shorter time scale $\tau_{\text{sp}} \propto a$. The destruction is stronger during the very initial phase $t \lesssim 50$ kyr when the ejecta is denser and hotter. Within $\sim 50 - 100$ kyr the maximum of $f_{M_d}(a_i)$ shifts by factor 2 toward smaller radii, on longer times between 100 and 300 kyr the sputtering rate slightly weakens because of a lower temperature in the ejecta.

Increase of the ambient gas density enhances dust sputtering. The resulted behavior can be qualitatively described as a shift of the size distribution function $f_{M_d}(a) \sim f_{M_d}(a/n)$ at a given time, as can be found from comparison of the distributions in Fig. 6 with the corresponding curves on Fig. 5.

3.2 Purity of the background and injected dust

The overall dynamics of dust destruction in either cases – the background and the injected particles, is predominantly determined by the interrelation between the collisional coupling (stopping) time τ_s , the sputtering time τ_{sp} and the local sound time $t_{\text{sound}} = \Delta x/c_s$, i.e. the crossing time of a cell where a given dust particle is currently situated. By order of magnitudes the stopping time $\tau_s \sim \rho_m a / \rho_g \sigma_t$ (Sec. A2),

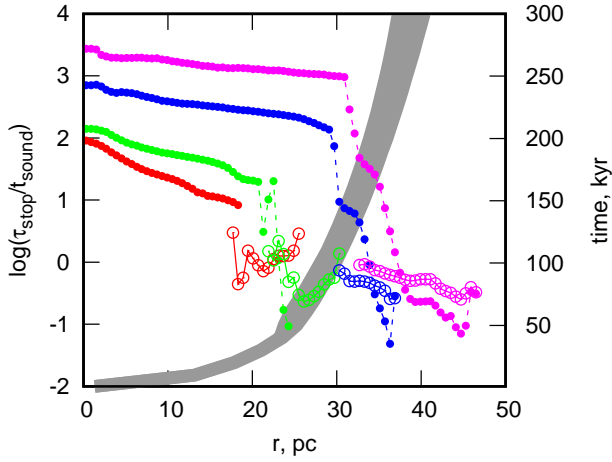


Figure 7. The averaged radial profiles for the averaged ratio of the grain stopping time of the injected and background dust to the local sound time t_{sound} , $a_0 = 0.1 \mu\text{m}$. Solid lines with open symbols are for the background dust, dashed lines with filled symbols are for the injected particles. Shaded band represents evolution of the bubble shell with the right border corresponding to the forward front where the gas velocity jumps, and the left one shows the border where the gas temperature $T \geq 10^5 \text{ K}$; at $t \lesssim 40 \text{ kyr}$ when the SN remnant is adiabatic the borders practically coincide, the time is shown on the right y-axis.

the thermal sputtering time at $T \gtrsim 10^6 \text{ K}$ is $\tau_{\text{sp}} \sim \rho_m a / n_g m_T \sigma_t$, m_T is the mass of a target particle (Draine 1995). As can be inferred from Fig. 1 the ratio $\tau_{\text{sp}}/\tau_s \sim m_H/m_T \lesssim 0.1$ for $m_T \gtrsim 10$. The background particles are destroyed mostly while they pass through out the shell. Within the shell they relax to the postshock gas flow as $\tau_s/t_{\text{sound}} \approx 1$ (Fig. 7), and only negligible fraction of them penetrate deeper into the hot bubble and ejecta. This is seen from dust density radial profiles in Fig. 1, where the amount of the survived background dust beneath the shell at $t \gtrsim 50 \text{ kyr}$ falls below 7% as observed in Fig. 8.

During the evolution the injected and background dust remain practically isolated: the one being locked in the ejecta and the hot bubble, the other is swept up into the shell. Only a minor fraction of the background dust can pervade deep in the bubble interior under conditions of weak collisional coupling $\tau_s/t_{\text{sound}} \gg 1$. Mild signs of intermixing can occur only in a thin layer deeply behind the shock front, as can be seen on radial distributions of dust density in Fig. 1.

The tendency of the injected and the background dust to stay in the remnant fairly unmixed can also be seen in Fig. 8, where the radial profiles of their abundances are given at different times. Both the background and the injected dust-to-gas ratios D are normalized to the initial value $D_0 = 10^{-2+[Z/H]}$ of the background dust. As the dust-to-gas ratio of injected dust is set $\zeta_{ej} = 1/30$ (see in Sec. 2), its normalized DtG ratio in the lower panel of Fig. 8 for $[Z/H] = -1$ is higher than in the upper panel for $[Z/H] = 0$. At $t = 50 \text{ kyr}$, the injected dust stays in the thermalized bubble interior with a considerable fraction of it being already destroyed, ~ 0.8 . During further expansion on next 150 kyr dust destruction weakens: at $t > 100 \text{ kyr}$ around 8–9 % of the injected dust particles survive, at $t \gtrsim 300 \text{ kyr}$ the injected dust practically merges to the shell and the survived dust fraction falls below $\sim 5\%$; no injected dust particles are observed to penetrate beyond the forward shock. The background dust is destroyed behind the shock efficiently only at early stages $t \lesssim 100 \text{ kyr}$, while at later stages the post-shock gas cools radiatively and temperature falls below the sputtering threshold. In both cases of high

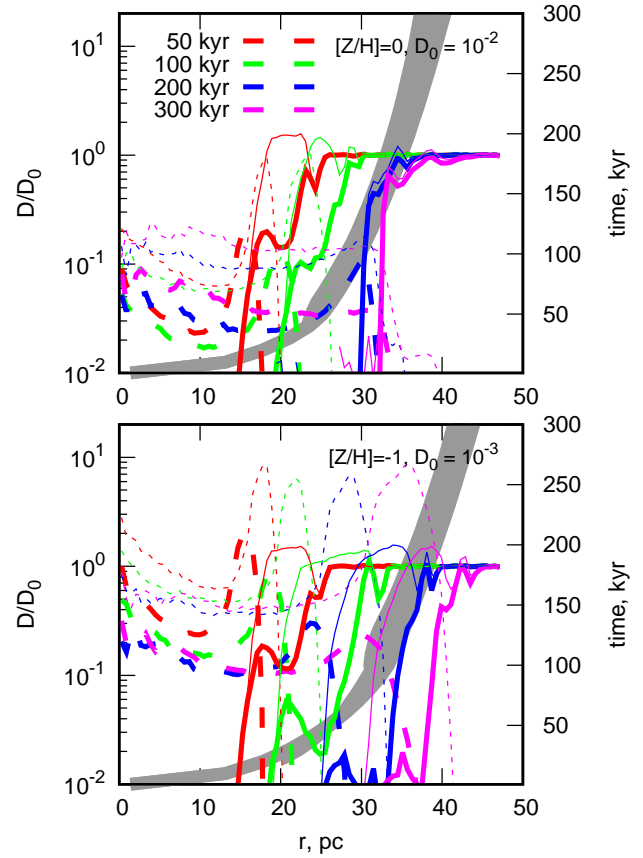


Figure 8. The radial distribution of the normalized dust density (i.e. the dust-to-gas ratio D normalized to the initial background value $D_0 = 10^{-2+[Z/H]}$) at times 50, 100, 200 and 300 kyr (color lines). Solid lines show the background dust: thin lines represent the case without dust destruction, thick lines illustrate the case when destruction is accounted. Dashed lines depict the injected dust: thin lines show dust without destruction, whereas the thick ones are for dust with destruction being accounted. Shaded area represents the evolution of the bubble shell as defined in Fig. 7 Upper panel shows the model with ambient gas of metallicity $[Z/H] = 0$ and $\zeta_d = 10^{-2}$, lower panel is for $[Z/H] = -1$ and correspondingly $\zeta_d = 10^{-3}$, the injected dust mass is $M_d = 1 M_\odot$ in both cases.

and low metallicity of ambient gas: $[Z/H] = 0$ and $[Z/H] = -1$, intermixing between the injected and the background particles is seen in a rather narrow region inward the bubble. While the injected particles even strongly depleted tend to occupy practically the entire bubble, the background ones penetrate inwards until being involved into expanding remnant gas $|v_p - v_{\text{gas}}| \ll \sigma_t$. As $\tau_{\text{sp}}/\tau_s \lesssim 0.1$ only a negligible amount of background dust can survive deep into the hot bubble interior, resulting in a sharp drop of their abundance seen in Fig. 8.

4 DISCUSSION AND CONCLUSION

Spatial variations of the extinction law in the Milky Way due to contribution from the SN injected and processed dust depend on the local gas density in ambient medium and the local SN rate. For ambient gas density $n \geq 0.1 \text{ cm}^{-3}$ only $\approx 13\%$ of ejected dust particles with radii $a \sim 0.1 \mu\text{m}$ do survive; at higher n this fraction decrease as $n^{-1.2}$. On the other hand, the estimates of the dust budget for a SN remnant at its radiative stages, $t \gtrsim 30 n^{-1/3} \text{ kyr}$, show that upto $\sim 80\%$ of the swept up background dust survives.

Therefore, after $t \geq 30n^{-1/3}$ kyr, the remnant contains the mass of the survived swept up dust upto $\geq 0.8M_{d,bk}^{swept} \sim 32 M_{\odot}$. On the other hand, the mass of the survived injected dust in the remnant is only $\leq 0.13M_{d,in}$, which results in the ratio of ejected-to-background dust in the remnant at its later stages of $M_{d,in}/M_{d,bk} \geq 0.004$, being too low to be recognized.

Dust supply from SN explosions in galaxies at $z < 5$ plays apparently a minor role, particularly when the small dust particles with $a < 0.1 \mu\text{m}$ are concerned. The survival percentage of $a \gtrsim 0.1 \mu\text{m}$ dust for high density environment $n > 1 \text{ cm}^{-3}$ is less than 10%. This estimate is qualitatively consistent with early consideration by Nozawa et al. (2006, 2007). This percentage of particles of small sizes is much lower than 1% in a $n \gtrsim 1 \text{ cm}^{-3}$ environment. Our results show that the survival fraction of dust particles of $a \sim 0.1 \mu\text{m}$ is $f_{d,surv} \sim 10^{-2} \bar{M}_{ej,d} n^{-\beta}$, n is the ambient density in cm^{-3} , $\beta > 1$, $\bar{M}_{ej,d}$ is the dust mass injected by a single SN. This results in an estimate of dust supply rate due to SN

$$\dot{M}_{\text{dust}}^+ \sim 10^{-4} \bar{M}_{ej,d} n^{-\beta} \text{ SFR } M_{\odot} \text{ yr}^{-1}, \quad (2)$$

here $\bar{M}_{ej,d}$ is in $1 M_{\odot}$, SFR is the SF rate in $1 M_{\odot} \text{ yr}^{-1}$, for the specific per mass supernova rate $\bar{v}_{sn} \sim 10^{-2} M_{\odot}$. For comparison, the typical number for the SN dust destruction rate in the Milky Way is (see, e.g., in Draine 2009)

$$\dot{M}_{\text{dust}}^- \sim 0.5 \text{ SFR}_5 M_{\odot} \text{ yr}^{-1}. \quad (3)$$

This conclusion seems to be applied particularly for dust production at the “cosmic noon” epoch because of an efficient destruction of the injected dust in the ejecta itself at a higher density environment.

SN explosions as the dust factory in galaxies is important only for $z > 5$ galaxies. Moreover, in most distant galaxies at $z > 10$ only large (grey) dust can survive extensive sputtering in SN shocks, because of their on average higher density environment $\propto (1+z)^3$. Estimates of the global dust budget in the ISM of high-redshift galaxies have to take into account highly sensitive sputtering yields on the shock velocity and ambient gas density, particularly when small dust particles are concerned. At such conditions, a general view that SN explosions in high- z galaxies are exceptionally selective with respect to a preferential destruction of small size dust particles.

ACKNOWLEDGEMENTS

We thank Biman B. Nath for valuable comments. Numerical simulations of the bubble dynamics were supported by the Russian Science Foundation (project no. 23-22-00266). YS acknowledges the hospitality of the Raman Research Institute.

DATA AVAILABILITY

The data underlying this article are available in the article.

REFERENCES

Arendt R. G., Dwek E., Kober G., Rho J., Hwang U., 2014, *ApJ*, 786, 55
 Baines M. J., Williams I. P., Asebiomo A. S., 1965, *MNRAS*, 130, 63
 Beelen A., Cox P., Benford D. J., Dowell C. D., Kovács A., Bertoldi F., Omont A., Carilli C. L., 2006, *ApJ*, 642, 694
 Bertoldi F., Carilli C. L., Cox P., Fan X., Strauss M. A., Beelen A., Omont A., Zylka R., 2003, *A&A*, 406, L55
 Bianchi S., Schneider R., 2007, *MNRAS*, 378, 973

Bocchio M., Marassi S., Schneider R., Bianchi S., Limongi M., Chieffi A., 2016, *A&A*, 587, A157
 Draine B. T., 1995, *Ap&SS*, 233, 111
 Draine B. T., 2009, in Henning T., Grün E., Steinacker J., eds, *Cosmic Dust - Near and Far Vol. 414 of Astronomical Society of the Pacific Conference Series, Interstellar Dust Models and Evolutionary Implications*. p. 453
 Draine B. T., 2011, *Physics of the Interstellar and Intergalactic Medium*. Princeton University Press
 Draine B. T., Salpeter E. E., 1979a, *ApJ*, 231, 438
 Draine B. T., Salpeter E. E., 1979b, *ApJ*, 231, 77
 Dwek E., Cherchneff I., 2011, *ApJ*, 727, 63
 Epstein P. S., 1924, *Physical Review*, 23, 710
 Ferrara A., Peroux C., 2021, *MNRAS*, 503, 4537
 Fitzpatrick E. L., Massa D., 1990, *ApJS*, 72, 163
 Gall C., Hjorth J., Andersen A. C., 2011, *A&ARv*, 19, 43
 Gomez H. L., Krause O., Barlow M. J., Swinyard B. M., Owen P. J., Clark C. J. R., Matsuura M., Gomez E. L., Rho J., Besel M. A., Bouwman J., Gear W. K., Henning T., Ivison R. J., Polehampton E. T., Sibthorpe B., 2012, *ApJ*, 760, 96
 Indebetouw R., Matsuura M., Dwek E., Zanardo G., Barlow M. J., Baes M., Bouchet P., Burrows D. N., Chevalier R., Clayton G. C., Fransson C., Gaensler B., Kirshner R., Lakićević M., Long K. S., Lundqvist P., Martí-Vidal I., Marcaide J., McCray R., Meixner M., Ng C. Y., Park S., Sonneborn G., Staveley-Smith L., Vlahakis C., van Loon J., 2014, *ApJ*, 782, L2
 Jones A. P., Tielens A. G. G. M., Hollenbach D. J., 1996, *ApJ*, 469, 740
 Kirchschlager F., Mattsson L., Gent F. A., 2022, *MNRAS*, 509, 3218
 Kirchschlager F., Schmidt F. D., Barlow M. J., Fogerty E. L., Bevan A., Priestley F. D., 2019, *MNRAS*, 489, 4465
 Klingenberg C., Schmidt W., Waagan K., 2007, *Journal of Computational Physics*, 227, 12
 Lewis G. M., Austin P. H., 2002, in 11th Conference on Atmospheric Radiation, American Meteorological Society Conference Series, eds. G. Smith, and J. Brodie, pp 1–4
 Maiolino R., Schneider R., Oliva E., Bianchi S., Ferrara A., Mannucci F., Pedani M., Roca Sogorb M., 2004, *Nature*, 431, 533
 Matsuura M., Dwek E., Barlow M. J., Babler B., Baes M., Meixner M., Cernicharo J., Clayton G. C., Dunne L., Fransson C., Fritz J., Gear W., Gomez H. L., Groenewegen M. A. T., Indebetouw R., Ivison R. J., Jerkstrand A., Lebouteiller V., Lim T. L., Lundqvist P., Pearson C. P., Roman-Duval J., Royer P., Staveley-Smith L., Swinyard B. M., van Hoof P. A. M., van Loon J. T., Verstappen J., Wesson R., Zanardo G., Blommaert J. A. D. L., Decin L., Reach W. T., Sonneborn G., Van de Steene G. C., Yates J. A., 2015, *ApJ*, 800, 50
 Mattsson L., 2021, *Research Notes of the American Astronomical Society*, 5, 288
 McKee C., 1989, in Allamandola L. J., Tielens A. G. G. M., eds, *Interstellar Dust Vol. 135, Dust Destruction in the Interstellar Medium*. p. 431
 Micelotta E. R., Matsuura M., Sarangi A., 2018, *Space Sci. Rev.*, 214, 53
 Mignone A., Flock M., Vaidya B., 2019, *ApJS*, 244, 38
 Moseley E. R., Teyssier R., Draine B. T., 2023, *MNRAS*, 518, 2825
 Nath B. B., Laskar T., Shull J. M., 2008, *ApJ*, 682, 1055
 Nozawa T., Kozasa T., Habe A., 2006, *ApJ*, 648, 435
 Nozawa T., Kozasa T., Habe A., Dwek E., Umeda H., Tominaga N., Maeda K., Nomoto K., 2007, *ApJ*, 666, 955
 Péroux C., De Cia A., Howk J. C., 2023, *MNRAS*, 522, 4852
 Priestley F. D., Chawner H., Barlow M. J., De Looze I., Gomez H. L., Matsuura M., 2022, *MNRAS*, 516, 2314
 Priestley F. D., Chawner H., Matsuura M., De Looze I., Barlow M. J., Gomez H. L., 2021, *MNRAS*, 500, 2543
 Slavin J. D., Dwek E., Jones A. P., 2015, *ApJ*, 803, 7
 Slavin J. D., Dwek E., Mac Low M.-M., Hill A. S., 2020, *ApJ*, 902, 135
 Sugerma B. E. K., Ercolano B., Barlow M. J., Tielens A. G. G. M., Clayton G. C., Zijlstra A. A., Meixner M., Speck A., Gledhill T. M., Panagia N., Cohen M., Gordon K. D., Meyer M., Fabbri J., Bowey J. E., Welch D. L., Regan M. W., Kennicutt R. C., 2006, *Science*, 313, 196
 Todini P., Ferrara A., 2001, *MNRAS*, 325, 726
 Toro E., 2009, *Riemann Solvers and Numerical Methods for Fluid Dynamics*:

A Practical Introduction. Springer Berlin Heidelberg

- Vaidya B., Mignone A., Bodo G., Rossi P., Massaglia S., 2018, *ApJ*, 865, 144
 Vasiliev E. O., 2011, *MNRAS*, 414, 3145
 Vasiliev E. O., 2013, *MNRAS*, 431, 638
 Vasiliev E. O., Nath B. B., Shchekinov Y., 2015, *MNRAS*, 446, 1703
 Vasiliev E. O., Shchekinov Y. A., Nath B. B., 2017, *MNRAS*, 468, 2757
 Vasiliev E. O., Shchekinov Y. A., Nath B. B., 2019, *MNRAS*, 486, 3685
 Weidenschilling S. J., 1977, *MNRAS*, 180, 57
 Wesson R., Bevan A., 2021, *ApJ*, 923, 148
 Youdin A., Johansen A., 2007, *ApJ*, 662, 613
 Zhu H., Slane P., Raymond J., Tian W. W., 2019, *ApJ*, 882, 135

APPENDIX A: DYNAMICS OF DUST PARTICLES

Here we describe an implementation of the particle dynamics in our gasdynamic code (Vasiliev et al. 2015, 2017, 2019). This code is based on the unsplit total variation diminishing (TVD) approach that provides high-resolution capturing of shocks and prevents unphysical oscillations. We have implemented the Monotonic Upstream-Centered Scheme for Conservation Laws (MUSCL)-Hancock scheme and the Haarten-Lax-van Leer-Contact (HLLC) method (see e.g. Toro 2009) as approximate Riemann solver. This code has successfully passed the whole set of tests proposed in Klingenberg et al. (2007). Several additional tests have been given in the appendix of Vasiliev et al. (2017).

Our description of dust dynamics basically follows to the method proposed by Youdin & Johansen (2007), several parts are similar to Mignone et al. (2019) and Moseley et al. (2023). In addition, we add several points allow to discriminate between sorts of particles, to follow the evolution of dust (macroscopic) mass, we include destruction processes due to thermal and kinetic sputtering. Due to we are going to study gas-dominated (by mass) flows in the ISM, we use explicit methods for solving the equations of dust dynamics.

A1 Properties

Dust particles trace the motion of grains in a gas. They are suffered by drag force from a gas, and due to it they transfer momentum and heat to a gas. Also they may be exposed to other external forces like gravity, radiation and so on.

Each dust particle is described by several features allow one to identify its evolution and physical properties, namely, color, time of injection, sort, size and mass. Two former can be used to identify a source of this particle. Dust particles can consist of different material – a sort of particle, e.g. from carbon or silicate. They can be of various sizes, which are distributed according to a power-law spectrum or have a single size. In the former case the dust is initially polydisperse and one can choose several sizes distributed by any spectrum. In the latter it is monodisperse, but due to possible destruction processes it may be evolved into polydisperse. These features are microscopic.

To follow the transport of dust mass (not of an individual grain) in a gaseous flow we introduce a macroscopic mass of a ‘superparticle’ or macroparticle. In this approach a particle is a conglomerate of microscopic grains. This value of mass (or supermass) is used to find the dust-to-gas mass ratio and so on. If it is necessary, any other feature of dust particle can be added.

A2 Dynamics

The dust component is modeled as an ensemble of macroparticles governed by the system of ODEs:

$$\frac{d\mathbf{x}_p}{dt} = \mathbf{v}_p \quad (\text{A1})$$

$$\frac{d\mathbf{v}_p}{dt} = \mathbf{a}_p - \frac{\mathbf{v}_p - \mathbf{v}_g}{\tau_s} \quad (\text{A2})$$

where \mathbf{x}_p and \mathbf{v}_p are the dust particle position and velocity vectors, \mathbf{a}_p is the acceleration vector of external forces (excepting gas-grain drag force), the stopping time is written for the Epstein drag with the supersonic Baines correction Epstein (1924); Baines et al. (1965); Draine & Salpeter (1979a):

$$\tau_s = \frac{m_p}{\pi a^2 \rho_{gas} \xi |\mathbf{v}_p - \mathbf{v}_{gas}|}, \quad (\text{A3})$$

where m_p , a_p and \mathbf{v}_p are the mass, size and velocity of a dust particle, respectively, ρ_{gas} and \mathbf{v}_{gas} are the density and velocity of gas, and the correction is

$$\xi = \left[1 + \frac{128 k_B T_{gas}}{9 \pi m_H (v_p - v_{gas})^2} \right]^{1/2} \quad (\text{A4})$$

where k_B is the Boltzmann constant, T_{gas} is the temperature of gas, m_H is the mass of the proton.

Due to the stopping time may be short enough compared to the gasdynamic timestep the system becomes stiff and then one should use implicit or semi-implicit schemes for solving it (see e.g., Vaidya et al. 2018; Moseley et al. 2023). This controls by the relation between the gasdynamic time (including the cooling time if necessary) and the stopping time, in the Epstein regime it is easily written as

$$\tau_s \approx \frac{\rho_m a}{\rho_g \sigma_T} \quad (\text{A5})$$

where ρ_m is the density of a solid particle’s material, a is the size of a particle, ρ_g is the density of the gas, σ_T is the mean thermal velocity. So that the transition to the stiff ODEs depends on the physical conditions and aims of simulation. In the diffuse interstellar medium with number density of 1 cm^{-3} and temperature of 10^4 K the stopping time of small particles with $a \lesssim 10^6 \text{ cm}$ is around 10^5 yrs . In a hot gas of SN interiors it drops to quite short value of $\sim 10^2 - 10^3 \text{ yrs}$ for $n_g \sim 10^{-1} - 10^{-2} \text{ cm}^{-3}$ and $T \sim 10^8 \text{ K}$ at early free expansion phase. This time scale is around the Courant time for the cell of 1 pc with the same physical conditions. Then, one can assume that such small particles are coupled with gas when its stopping time is shorter than the gasdynamic timestep. More exactly, small particles with short enough stopping time follow the gas as Lagrangian trace particles. In this approach the system of ODEs for the particle dynamics can be solved using the explicit ‘predictor-corrector’ stencil adopted in the code.

For particles we have implemented periodic, outflow and reflectory boundary conditions. They are similar to those for gas.

A3 Back-reaction to the gas

The drag force of a grain is proportional to the relative velocity between gas and particles Weidenschilling (1977):

$$\mathbf{f}_d = -\rho_d \frac{\mathbf{v}_g - \mathbf{v}_d}{\tau_s} \quad (\text{A6})$$

where \mathbf{v}_g , \mathbf{v}_d are the velocities of gas and dust particle, τ_s is the stopping (friction) time, for which we have implemented several regimes:

the constant stopping time, the Epstein drag, and the Epstein drag with the supersonic Baines correction [Epstein \(1924\)](#); [Baines et al. \(1965\)](#); [Draine & Salpeter \(1979a\)](#). Usually we use the latter.

In the total energy equation we need to take into account the work done by the drag force and the frictional heating due to dust:

$$\mathbf{v}_d \mathbf{f}_d = \mathbf{v}_g \mathbf{f}_d + \rho_d \frac{(\mathbf{v}_d - \mathbf{v}_g)^2}{\tau_s} \quad (\text{A7})$$

The momentum and energy equations are added by source terms responsible for the back-reaction to the gas, see eqns [A6-A7](#):

$$\frac{\partial(\rho_{gas} \mathbf{v}_{gas})}{\partial t} + \dots = \dots + \mathbf{f}_d, \quad (\text{A8})$$

and

$$\frac{\partial E_{gas}}{\partial t} + \dots = \dots + \mathbf{v}_d \mathbf{f}_d. \quad (\text{A9})$$

A4 Destruction

During its moving through a gas dust particles can be destructed by both thermal and kinetic sputtering ([Draine & Salpeter 1979a](#)). We use the thermal sputtering rate from [Draine \(2011\)](#) and the kinetic one from [Nozawa et al. \(2006\)](#). For the latter we approximate the rate presented by [Nozawa et al. \(2006\)](#) in their Fig. 2b averaged over the target species:

$$\dot{a} = 4 \times 10^{-4} n_{gas} \exp\left(-\frac{4 \times 10^2}{|v_p - v_{gas}|}\right) |v_p - v_{gas}|^{-0.7} \mu\text{m yr}^{-1}, \quad (\text{A10})$$

where the velocities are in km/s.

For rough estimates of nonthermal destructions one can utilize the following equation for supersonic relative dust motion when the kinetic sputtering ([Draine 1995](#))

$$4\rho_m \frac{da}{dt} = -nm_t w Y(w), \quad (\text{A11})$$

with m_t is the target mass ($m_t \lesssim 20 - 30 m_p$), $w \equiv v_p - v_g$. Dividing Eq. (A11) over Eq. (A2) one gets

$$\frac{d \ln a}{d \ln w} = \frac{m_t Y(w)}{3m_H}, \quad (\text{A12})$$

and approximately

$$a \geq a_0 \left(\frac{w}{w_0}\right)^q \quad (\text{A13})$$

with $q = m_t \langle Y(w) \rangle / 3m_H$, $\langle Y(w) \rangle \approx 0.01$ being the mean value of the yield $Y(w)$ averaged over the target species in [Nozawa et al. \(2006\)](#) in the velocity range of interest $w = 100 - 500 \text{ km s}^{-1}$. This results in $a \geq 0.88 a_0$, or for mass depletion $m(a) \geq 0.7 m(a_0)$.

For injected dust particles the kinetic sputtering seems to be even weaker because they seem to be involved into the ejecta flow at initial “ejecta-dominated” stages with a low difference in relative velocities dust and gas and a relatively low $\tau_s \lesssim 1 \text{ kyr}$ in the ejecta, as mentioned in Sec. 2.

A5 Grid and particle’s quantities

For depositing a particle quantity q_p to the grid and interpolating fluid quantity Q_{ijk} at the particle location we use

$$Q_{ijk} = \sum_{p=1}^{N_p} W(\mathbf{x}_i - \mathbf{x}_p) q_p, \quad q_p = \sum_{ijk} W(\mathbf{x}_{ijk} - \mathbf{x}_p) Q_{ijk}, \quad (\text{A14})$$

where the kernel $W(\mathbf{x}_i - \mathbf{x}_p) = W(x_i - x_p)W(y_i - y_p)W(z_i - z_p)$ is product of three one-dimensional weight functions, and only neighbour cells give a nonzero contribution to the particle in the second sum. We have implemented traditional shape functions such as the “Nearest Neighbor Point” (NGP), “Cloud-In-Cell” (CIC), and “Triangular Shape Cloud” (TSC), we have adopted that each particle can give a nonzero contribution only to the computational zone hosting the particle, its left and right neighbours.

A6 Memory allocation

In our realization particles are held in a computer memory using a singly linked list consisting of sequentially linked structures. Each node contains the information about the current particle and the pointer to the next node in the sequence. In this list nodes can be inserted or removed. A particle is described by several individual features such as identitical number, three coordinates, three velocities, time moment of injection and so on.

APPENDIX B: TESTS

B1 Particle-gas deceleration test

We study the dynamical interaction of an ensemble of uniformly distributed dust particles with a homogeneous gas flow. Initially stationary particles are placed into a flow with a constant velocity $v_{g,0}$. Assuming fixed stopping time for particles we get an analytic solution for the evolution of particle velocity: $v_p(t) = v_{g,0} [1 - \exp(-t/\tau_s)]$.

In our test runs of the coupled particle-gas dynamics we set the gas flow velocity equal to $v_{g,0} = 10 \text{ km/c}$, and investigate the velocity of particles for different stopping times. Figure [B1](#) presents the particle velocity for $\tau_s = (1 - 4) \times 10^5 \text{ yr}$ for grid with number of cells along each spatial direction $N = 100, 200$ and 400 (color lines). One can see a good coincidence between our numerical results and the above-mentioned analytic solution (depicted by black dashed lines). Only for the coarse grid ($N = 100$) and the shortest stopping time one can mark small deviations from the analytic curve.

B2 SN evolution: a convergence

We follow the evolution of a single SN remnant with different spatial resolution for the grid and fixed number of dust particles injected by SN. The number of dust particles in the ambient gas (or background dust particles) is proportional to the grid resolution, because we set one such particle per grid cell. Figure [B2](#) presents the one-dimensional (along line of sight crossed the center of SN bubble) profile of the dust density depositing to the grid for different spatial resolution of the grid: from 1 to 0.1875 pc. The slice is for a SN bubble with age of 20 kyr. The number of injected particles remains the same and equal to 8 millions. For comparison the gas density profile along the same line of sight and for the highest spatial resolution (0.1875 pc) is added. The dust density is multiplied by a factor of 100 for better presentation (the dust-to-gas density relation in the ambient gas is initially set to 0.01). One can see that the dust distributions are close to each other and then we conclude that the grid resolution of 0.5 pc is sufficient to follow the dust dynamics during the SN bubble evolution. One can note gaps in lines for high grid resolution, that means there are no particles in these areas, this is because of limited number of particles. So that, when we plot a 1D slice for better spatial resolution, we may find no particle in cell.

Figure [B3](#) shows the one-dimensional distribution of dust density

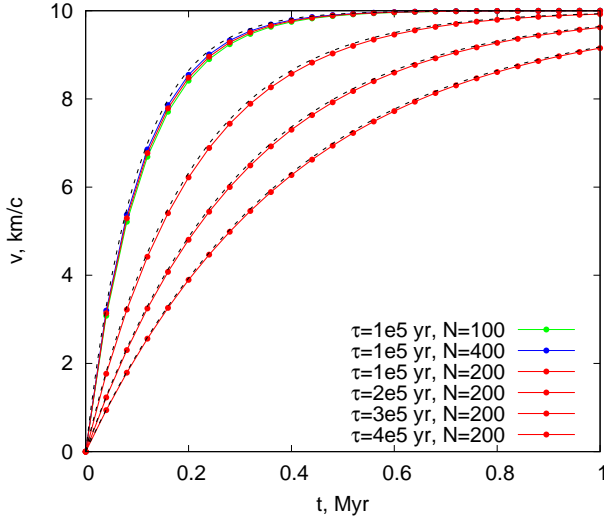


Figure B1. The velocity of dust particles for stopping times $\tau_s = 10^5$, 2×10^5 , 3×10^5 and 4×10^5 yr (red solid lines from top to bottom, respectively) in a homogeneous gas flow for grid with number of cells along each spatial direction $N = 200$. The green and blue lines show the velocity for $\tau_s = 10^5$ yr and number of cells $N = 200$ and 400. The black dash lines represent the analytic solution for stopping times $\tau_s = 10^5$, 2×10^5 , 3×10^5 and 4×10^5 yr (from top to bottom).

for the runs with different number of dust particles, i.e. 8, 16 and 32 millions, but the same grid resolution equal to 0.5 pc. The slice is for a SN bubble with age of 20 kyr. One can see that the density profiles of the dust are very close for the runs with different number of particles. Certainly, number of dust particles is decreased in the inner part of the bubble, where the gas density reaches the lowest value. During later evolution it is possible that there are no dust particles in this region especially for small initial number of particles. So that larger number of particles allow us to trace the dust evolution inside the most rarefied part of the ejecta.

Then, we can choose for our runs the following fiducial parameters: the spatial resolution is taken equal to 0.5 pc and the number of injected dust particles is adopted to 8 millions. These values are sufficient to follow the dust dynamics inside a SN bubble adequately.

B3 Dust-gas decoupling

Dust particles are initially deposited to the computational grid as described above in Sec. 2 and in Sec. A1. In dynamical regime dust particles can escape their 'mother' cells and move into neighbour ones, in those cases when the stopping time τ_s becomes longer than the crossing time for a grid cell t_{sound} , and the collisional coupling weakens, Sec. 3.2. As a result, depending on gas density and number of particles the overall distribution of dust particles can become patchy, with lack or deficient dust particles at certain regions of the bubble and in the averaged radial profiles. The middle panel of Fig. B4 presents the positions of dust particles in a 2D slice (a single cell in thickness) at a certain time after explosion. Initially the background dust particles are deposited to the computational grid homogeneously with a density of one particle per a cell in its centre, as seen in Fig. B4 in the unperturbed region. Evacuation of dust particles due to decoupling are clearly seen in several regions behind the front. Within the hydrodynamical description dust particles along with their physical characteristics mentioned in Sec. A5 are smeared out over the computational cell resulting in mitigation of this patchiness. This

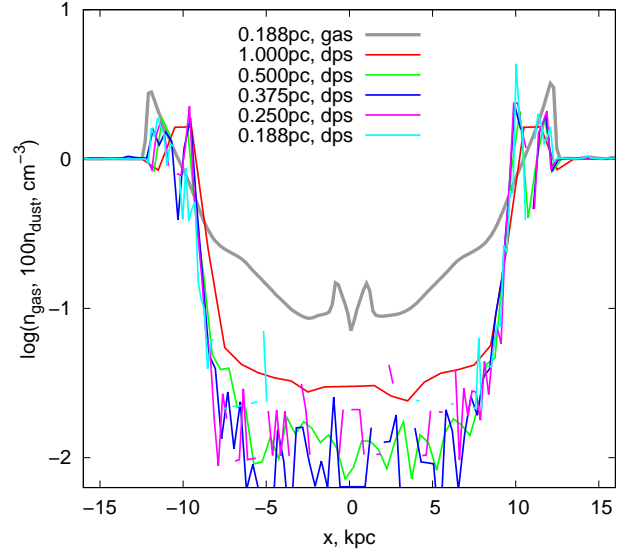


Figure B2. The one-dimensional profile of the dust density depositing to the grid for different spatial resolution of the grid: the color lines correspond to the cell size from 1 to 0.1875 pc. The slice is for a SN bubble with age of 20 kyr. The number of injected particles in all models is equal to 8 millions. The thick grey line depicts the gas density profile along the same line of sight and for the highest spatial resolution (0.1875 pc). The dust density is multiplied by a factor of 100.

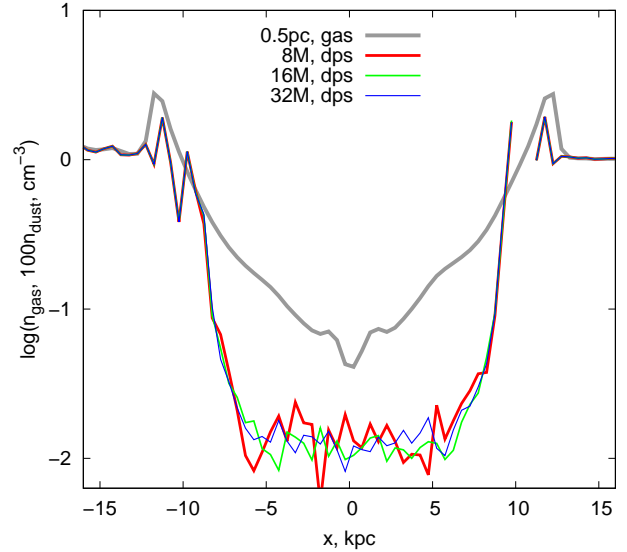


Figure B3. The one-dimensional slice of dust density for the runs with different number of dust particles: the color lines show the profiles for 8, 16 and 32 millions of particles. The grid resolution is the same and equal to 0.5 pc. The thick grey line depicts the gas density profile for this resolution. The age of a SN bubble is 20 kyr. The dust density is multiplied by a factor of 100.

manifests in squeezing the area with lacking dust, as seen in the right panel of Fig. B4). The radial profiles shown in Sec. 3.1 and Sec. 3.2 account this smearing out effect.

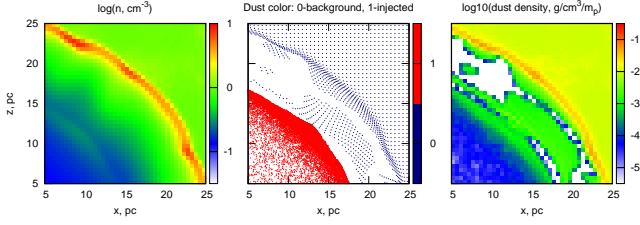


Figure B4. A part of the SN shell: 2D slices of the gas density (left), dust particles (middle), average dust density (right).

APPENDIX C: LAGRANGIAN PARTICLES

In addition, we have implemented in our code Lagrangian or tracing particles, which follow the gaseous flow and mark regions of a gas filled by injected 'fluid' without diffusion.

C1 Properties

In addition to several general features of particles needed to the identification and evolution each Lagrangian particle is described by its color and time of its birth or injection. For instance, a color can be used to identify a source of this particle.

C2 Dynamics

The dynamics of Lagrangian particles is modeled as an ensemble of particles governed by the system of ordinary differential equations (ODEs):

$$\frac{d\mathbf{x}_p}{dt} = \mathbf{v}_g \quad (\text{C1})$$

where \mathbf{v}_g is the gas velocity vector in the cell where a particle is located.

We solve this system coupled with the gasdynamic equations using the predictor-corrector scheme realized in the gasdynamic code.

For depositing a particle quantity q_p to the grid and interpolating fluid quantity Q_{ijk} at the Lagrangian particle location we use the same description as for dust particles.